

LEARNING DYNAMICALLY INSPIRED INVARIANT SUBSPACES FOR KOOPMAN AND TRANSFER OPERATOR APPROXIMATION

GARY FROYLAND* AND KEVIN KÜHL*

Abstract. Transfer and Koopman operator methods offer a framework for representing complex, nonlinear dynamical systems via linear transformations, enabling for a deeper understanding of the underlying dynamics. The spectrum of these operators provide important insights into system predictability and emergent behaviour, although efficiently estimating them from data can be challenging. We tackle this issue through the lens of general operator and representational learning, in which we approximate these linear operators using efficient finite-dimensional representations. Specifically, we machine-learn orthonormal, locally supported basis functions that are dynamically tailored to the system. This learned basis provides a particularly accurate approximation of the operator’s action as well as a nearly invariant finite-dimensional subspace. We illustrate our approach with examples that showcase the retrieval of spectral properties from the estimated operator, and emphasise the dynamically adaptive quality of the machine-learned basis.

Key words. Koopman Operator, Transfer Operator, Invariant Subspace, Spectrum

1. Introduction. Nonlinear dynamical systems emerge in a variety of domains, including biology, ecology, physics, and engineering; understanding their behaviour is critical for prediction and control. However, studying nonlinear systems is difficult due to their complex and frequently high-dimensional and chaotic behaviour. A promising approach is to study a nonlinear system via an associated linear operator acting on observables (functions of the state). In this operator-theoretic framework, the nonlinear evolution in state space is lifted to a linear (but infinite-dimensional) evolution in a function space. For example, given a discrete dynamical system $x_{n+1} = T(x_n)$ with state space X , one can define the transfer operator \mathcal{L} acting on a function $g : X \rightarrow \mathbb{R}$ by composition:

$$\mathcal{L}g := g \circ T^{-1}$$

The operator $\mathcal{L} : L^2(X) \rightarrow L^2(X)$ is linear even if T is nonlinear. By analysing \mathcal{L} , one can leverage linear techniques to understand nonlinear dynamics [9, 22, 10, 8, 15]. The trade-off is that \mathcal{L} typically acts on infinite-dimensional function spaces, and to study \mathcal{L} in practice we must work with finite-dimensional approximations.

A major challenge in typical applications is that we do not know *a priori* which observables or subspaces will yield a good finite-dimensional representation of \mathcal{L} . Many traditional approaches assume a predefined set of basis functions – e.g. monomials, Fourier modes, or the library of observables supplied to Extended Dynamic Mode Decomposition (EDMD) [27] – that may not be well suited to the system at hand. For example, data-driven approximations of the Koopman operator, such as DMD [25, 2] and its variations, depend on the user supplying observables that (approximately) span an invariant subspace under \mathcal{L} . If key observables are omitted, important dynamics can be missed, and a lack of invariance can contribute to estimation errors. Consequently, identifying coordinate transformations or feature spaces in which a nonlinear system behaves linearly remains an active and widely researched topic [16, 1, 11, 18].

Recent research has concentrated on learning suitable observables or invariant subspaces from data rather than defining them beforehand. Takeishi *et al.* [26] introduced a fully data-driven method to identify a Koopman-invariant subspace by

*School of Mathematics and Statistics, UNSW Sydney, Sydney NSW 2052, Australia. (g.froyland@unsw.edu.au, k.kuhl.oliveira@unsw.edu.au).

optimising over a class of candidate functions (represented by neural networks). Similarly, one can use deep learning to discover Koopman eigenfunctions by training an autoencoder whose latent variables evolve linearly in time [21]. Such an approach would yield intrinsic coordinates that linearize the dynamics.

In parallel, there has been significant progress in learning operators (maps between function spaces) directly using neural networks. This is built upon the universal approximation theorem for operators [6, 17], which extends the classic universal approximation property of neural nets from finite-dimensional functions to infinite-dimensional functionals. Lu *et al.* proposed the Deep Operator Network (DeepONet) [20] architecture. DeepONet consists of two subnetworks (a branch network that encodes the input function via evaluations at a fixed set of sensor points, and a trunk network that encodes the location x where the output is evaluated) and can learn nonlinear operator mappings. Another example is the Basis Operator Network (BasisONet) of Hua and Lu [14], which uses a neural-network-based dual autoencoder setting to learn a lower-dimensional representation (basis) for functions in the input and output function spaces. Over the past few years, different architectures have been proposed for various scenarios, including Fourier Neural Operators [19] and PCA-Net [3]. A comprehensive review of operator learning techniques may be found in [4], including insightful parallels to the matrix recovery problem.

Despite this progress, there remains a gap in jointly learning the operator and an invariant subspace tailored to that operator. In this work, we propose a neural-network architecture that simultaneously learns an approximation of the transfer operator \mathcal{L} and a set of basis functions with desirable numerical properties (such as orthonormality and local support) that span a nearly invariant subspace of $L^2(X)$. Our learned basis automatically adapts to the dynamics to create highly efficient (in terms of basis functions required) and accurate bases for finite-dimensional representations of the transfer operator. We mainly discuss the transfer operator, but all statements also hold for the Koopman operator.

An outline of the paper is as follows. Section 2 introduces the Single Autoencoder Basis Operator Network (SABON) and proves a universal-approximation theorem for the presented setting. Section 3 validates SABON, first on a circle-rotation map—showing that spectral properties of the transfer operator can be recovered from the learned basis and approximator—and second on a perturbed Arnold cat map, where the basis adapts to the anisotropic dynamics and outperforms an equal-cardinality Fourier basis. The final section discusses the main findings and sketches directions for future work.

2. Methodology. We introduce notation that will be useful throughout the paper. Let the state space (X, \mathcal{B}, μ) be a probability space with X compact, and let $T: X \rightarrow X$ a measure-preserving transformation. We consider $\{x_i\}_{i=1, \dots, n} \subset X$ to be a discretization of the state space, for example a set of grid or sampling points. An observable $g \in L^2(X)$ is represented by its values on this grid, that is $[g(x_1), g(x_2), \dots, g(x_n)]^\top$. The action of the transfer operator produces a new map $\mathcal{L}(g)$, whose values on the grid are $[(\mathcal{L}g)(x_1), \dots, (\mathcal{L}g)(x_n)]^\top$. If $V \subset L^2(X)$ is a finite-dimensional invariant subspace spanned by basis functions ϕ_1, \dots, ϕ_N , then the restriction of \mathcal{L} to V can be represented by an $N \times N$ matrix L such that $\mathcal{L}\phi_j = \sum_{k=1}^N L_{kj}\phi_k$. If V is not \mathcal{L} -invariant, a finite-dimensional approximation $\hat{\mathcal{L}}$ is often obtained by first applying \mathcal{L} to the basis elements of V and then projecting the resulting functions back into V . The quality of this approximation depends on the choice of subspace V . Two main components are the richness of the space V and the

error incurred due to projection into V . The latter error is greatly reduced if V is approximately invariant under \mathcal{L} . Invariant (or approximately invariant) subspaces thus play a key role in accurately approximating \mathcal{L} .

We will adopt the standard convention of scalar feed-forward neural networks as a composition of affine maps and nonlinear activations, $\phi: \mathbb{R}^d \rightarrow \mathbb{R}$. Stacking Q such networks gives a vector-valued network $\psi: \mathbb{R}^d \rightarrow \mathbb{R}^Q$, written as

$$\hat{\phi}(x) = (\phi_1(x), \dots, \phi_Q(x))^\top$$

Finally, we call the collection $\{\phi_1, \dots, \phi_N\}$ a *neural basis* for the finite-dimensional subspace $V = \text{span}\{\phi_j\}_{j=1}^N \subset L^2(X)$.

2.1. Single Autoencoder Basis Operator Networks (SABON). To address the problem of simultaneously learning an approximator to the Transfer Operator and a suitable invariant subspace, we propose the following architecture composed of a single autoencoder and a standard neural network.

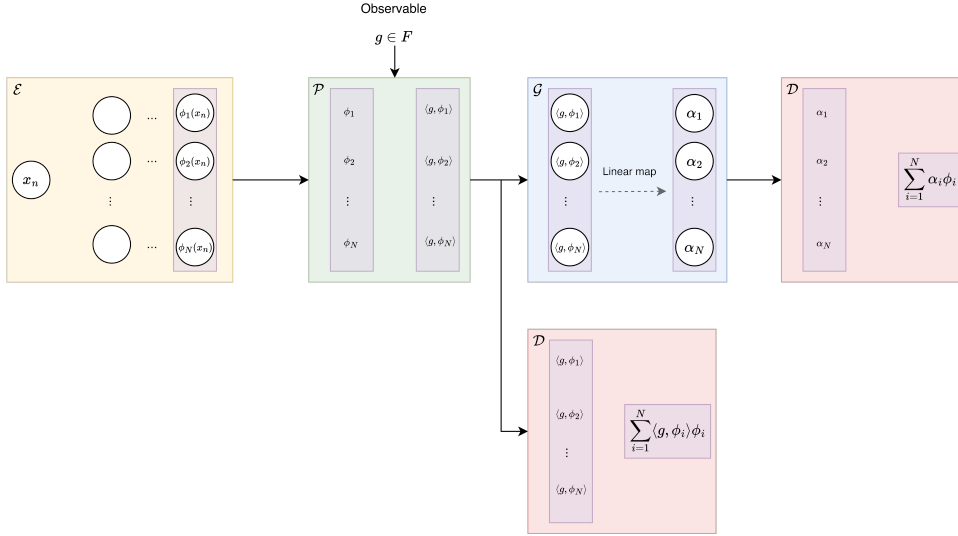


Fig. 1: SABON consists of an encoder, a latent projection, two identical decoders, and a linear map \mathcal{G} . The encoder learns basis functions $\{\phi_j\}_{j=1}^N$, while $\mathcal{G}: \mathbb{R}^N \rightarrow \mathbb{R}^N$ approximates the action of $\hat{\mathcal{L}}(g)$ on $V = \text{span}\{\phi_j\}_{j=1}^N$. Using two decoders - one for g and one for $\hat{\mathcal{L}}(g)$ - enforces a basis that is suitable for representing both observables and their transformed counterparts.

Two inputs are needed for the above architecture: the observable function g , represented by its evaluation over the sampling points $[g(x_1), g(x_2), \dots, g(x_n)]^\top$ and the discretization $\{x_i\}_{i=1, \dots, n} \subset X$, where all maps are evaluated. We explain the SABON components in turn.

Encoder (\mathcal{E}). The encoder in SABON is a vector-valued neural network

$$\hat{\phi}: \mathbb{R}^n \longrightarrow \mathbb{R}^N$$

that sends the grid vector $[g(x_1), \dots, g(x_n)]^\top$ to the evaluations

$$[\phi_1(x_1), \dots, \phi_N(x_n)]^\top$$

Its N scalar components $\{\phi_j\}_{j=1}^N$ form the learned neural basis of the subspace V introduced above.

Projection (\mathcal{P}). The projection block computes $\{\langle g, \phi_j \rangle\}_{j=1, \dots, N}$ for an observable $g \in L^2(X)$ and a set of learned basis functions $\{\phi_j\}_{j=1}^N$. In more general terms, we define $\mathcal{P}_{\{\phi_j\}_{j=1}^N} : L^2(X) \rightarrow \mathbb{R}^N$ via

$$(2.1) \quad \mathcal{P}_{\{\phi_j\}_{j=1}^N}(g) = (\langle g, \phi_1 \rangle, \dots, \langle g, \phi_N \rangle)$$

We shall omit the subscript of \mathcal{P} throughout the rest of the paper.

Map \mathcal{G} in latent space. The action of the transfer/Koopman operator is learned in the form of a linear map on block \mathcal{G} . The coefficients $\langle g, \phi_j \rangle$, $j = 1, \dots, N$ in the latent space are input to the subnetwork \mathcal{G} , which learns the action of $\hat{\mathcal{L}}$ in the latent space. That is, the block \mathcal{G} consists of a learnable linear map capable of transforming the expanding coefficients of g on $\{\phi_j\}_{j=1}^N$ into the expanding coefficients of $\hat{\mathcal{L}}(g)$ onto the same basis.

Decoder \mathcal{D} . The architecture employs two identical decoder instances: (i) the upper decoder that reconstructs the transformed observable $\hat{\mathcal{L}}(g)$, and (ii) the lower decoder that reconstructs the original observable g shown at the bottom of the diagram. Given the latent coefficients $c_j := \langle g, \phi_j \rangle$, the lower decoder produces

$$\hat{g}(x) = \sum_{j=1}^N c_j \phi_j(x),$$

which, for an orthonormal basis $\{\phi_j\}_{j=1}^N$, is the orthogonal projection of g onto $V = \text{span}\{\phi_j\}_{j=1}^N$. In that same spirit, the upper decoder receives the coefficients $(\alpha_1, \dots, \alpha_N)$ supplied by the block \mathcal{G} (defined next) and reconstructs

$$\hat{\mathcal{L}}(g)(x) = \sum_{j=1}^N \alpha_j \phi_j(x).$$

Because they share the same functional form, we introduce the generic decoder $\mathcal{D}_{\{\phi_j\}_{j=1}^N} : \mathbb{R}^N \rightarrow L^2(X)$ as

$$\mathcal{D}_{\{\phi_j\}_{j=1}^N}(a_1, \dots, a_N) = \sum_{j=1}^N a_j \phi_j$$

To simplify the notation, we will also omit the subscript in the sequel. The coefficients serving as input to \mathcal{D} will always be clear from the context (i.e. which maps are composed with \mathcal{D}).

Both decoders will appear in the loss term: the lower one is used in the reconstruction loss for the observable g , while the decoder in the top row is considered in the reconstruction loss for the transformed observable $\hat{\mathcal{L}}(g)$. This enforces that the learned basis $\{\phi_j\}_{j=1}^N$ is simultaneously well suited for expanding the observable itself and the action of the operator on that observable.

One of the key features of basis operator networks is that they simultaneously optimise the learned subspace and the operator action. This is performed through a suitable loss function, adapted from [14] to include a sparsity penalty that enforces local support of the basis functions. The loss function has three components (in practice these are evaluated with discretized versions):

1. The deviation of the autoencoder blocks from the identity are optimised with the relative L_2 loss with respect to the identity operator on $L^2(X)$ (Id).

$$(2.2) \quad \mathcal{E}_1(\mathcal{P}, \mathcal{D}, g) := \frac{\|Id(g) - \mathcal{D} \circ \mathcal{P}(g)\|_2}{\|Id(g)\|_2}.$$

2. The network \mathcal{G} , responsible for learning the projected action of \mathcal{L} on V has the loss term:

$$(2.3) \quad \mathcal{E}_2(\mathcal{L}, \mathcal{G}, \mathcal{P}, \mathcal{D}, g) := \frac{\|\mathcal{L}(g) - \mathcal{D} \circ \mathcal{G} \circ \mathcal{P}(g)\|_2}{\|\mathcal{L}(g)\|_2}.$$

3. The third term of the loss function is a sparsity penalty to encourage the learned basis functions to have local support

$$(2.4) \quad \mathcal{E}_3(\{\phi_j\}_{j=1}^N) = \frac{1}{N} \sum_{j=1}^N \|\phi_j\|_{L^1}.$$

The complete loss function is

$$(2.5) \quad J(\mathcal{L}, \mathcal{G}, Id, \mathcal{P}, \mathcal{D}, g) = \beta_1 \mathcal{E}_1(Id, \mathcal{P}, \mathcal{D}, g) + \beta_2 \mathcal{E}_2(\mathcal{L}, \mathcal{G}, \mathcal{P}, \mathcal{D}, g) + \beta_3 \mathcal{E}_3(\{\phi_j\}_{j=1}^N),$$

where $\beta_1, \beta_2, \beta_3 > 0$. Finally, we discuss the activation functions employed in the proposed architecture. For the \mathcal{G} network, which is learning the action of a linear operator (transfer or Koopman), we selected a linear activation function, namely the identity function, and set the bias term to zero. The activation functions for the encoder block (\mathcal{E}) can be chosen among the usual candidates, and we had the best results with ReLU in our experiments.

The combined architecture and loss in SABON are structured so that the learned basis $\{\phi_j\}_{j=1}^N$

- is locally supported, enforced by the sparsity term in the loss function;
- is approximately orthogonal;
- spans a subspace V that is (approximately) invariant under the Perron–Frobenius/Koopman operator;
- yields small projection error for any observable g , thanks to the loss term \mathcal{E}_1 ;
- and
- yields equally small projection error for the transformed observable $\hat{\mathcal{L}}(g)$, given the term \mathcal{E}_2 in the loss function.

Thus \mathcal{E}_2 simultaneously optimises for a good finite-dimensional approximation of the operator action and enforces that $\{\phi_j\}_{j=1}^N$ spans a space V well suited for representing $\hat{\mathcal{L}}(g)$. A final rescaling step yields an orthonormal basis.

2.2. Universal Approximation Theorem. Hua et al. (2023) [14] treat a general, possibly nonlinear, operator

$$\mathcal{J}: \mathcal{H}_{\text{in}} \longrightarrow \mathcal{H}_{\text{out}}, \quad \mathcal{H}_{\text{in}} \neq \mathcal{H}_{\text{out}}$$

and therefore employ two autoencoders to learn separate finite-dimensional subspaces for the domain and codomain.

In this work, we restrict ourselves to the transfer and Koopman operators associated with a measure-preserving dynamical system. Under these conditions, both operators satisfy

$$\mathcal{L}: L^2(X) \rightarrow L^2(X),$$

so only a single subspace $V \subset L^2(X)$ is required to approximate both the observable g and its image $\hat{\mathcal{L}}(g)$. Consequently, one should instead use a single encoder. We therefore state our approximation theorem in this alternate setting.

THEOREM 2.1. *Let $X \subset \mathbb{R}^d$ be compact and let $\mathcal{L}: L^2(X) \rightarrow L^2(X)$ be a continuous operator that is either the transfer or the Koopman operator associated with some measure-preserving dynamical system on X . Then for each compact set $\mathcal{K} \subset L^2(X)$ and any $0 < \epsilon < 1$ there exist $N > 0$, a neural basis $\phi = (\phi_1, \phi_2, \dots, \phi_N): X \rightarrow \mathbb{R}^N$ and a linear map $\mathcal{G}: \mathbb{R}^N \rightarrow \mathbb{R}^N$ such that the operator $A := \mathcal{D}_{\{\phi_j\}_{j=1}^N} \circ \mathcal{G} \circ \mathcal{P}_{\{\phi_j\}_{j=1}^N}$ satisfies*

$$\sup_{g \in \mathcal{K}} \|\mathcal{L}(g) - A(g)\|_{L^2(X)} \leq \epsilon.$$

Typical examples of compact sets $\mathcal{K} \subset L^2(X)$, with $X \subset \mathbb{R}^b$ ($b \in \mathbb{N}$), include the closed unit ball of any finite-dimensional subspace $\text{span}\{\chi_1, \dots, \chi_m\} \subset L^2(X)$ and - when X is a bounded Lipschitz domain (its boundary is locally a Lipschitz graph) - the closed unit ball of $H^1(X)$; the latter is compact in $L^2(X)$ by the Rellich–Kondrachov embedding

$$H^1(X) \hookrightarrow L^{p^*}(X), \quad p^* = \frac{2b}{b-2},$$

valid for suitable b , and for either choice of \mathcal{K} one can choose a radius $R > 0$ so that the spatial and Fourier integrals in [23, Theorem 3] are arbitrarily small.

Proof of Theorem 2.1. The proof proceeds almost exactly as in [14, Theorem 2.2], so we omit the repeated details and focus on the necessary modifications. First, we need only one neural basis ($\{\phi_1, \dots, \phi_N\} \subset L^2(X)$) for both the input and output spaces. The universal approximation property [14, Theorem 2.1] ensures we can approximate each $g \in \mathcal{K}$ by a finite-rank projection g^N , and the continuity of \mathcal{L} on an augmented compact set still supports a uniform-continuity argument just as in the original proof.

The main difference appears in the error decomposition. In [14], one bounds three terms to handle potentially different neural bases for input and output spaces, but here we merge everything into two terms. If $A := \mathcal{D}_{\{\phi_j\}_{j=1}^N} \circ \mathcal{G} \circ \mathcal{P}_{\{\phi_j\}_{j=1}^N}$, then for $g \in \mathcal{K}$

$$\begin{aligned} \|\mathcal{L}(g) - A(g)\|_{L^2(X)} &\leq \left\| \mathcal{L}(g) - \mathcal{D}_{\{\phi_j\}_{j=1}^N} \circ \mathcal{P}_{\{\phi_j\}_{j=1}^N} \circ \mathcal{L}(g) \right\|_{L^2(X)} \\ &\quad + \left\| \mathcal{D}_{\{\phi_j\}_{j=1}^N} \circ \mathcal{P}_{\{\phi_j\}_{j=1}^N} \circ \mathcal{L}(g) - \mathcal{D}_{\{\phi_j\}_{j=1}^N} \circ \mathcal{G} \circ \mathcal{P}_{\{\phi_j\}_{j=1}^N}(g) \right\|_{L^2(X)}, \end{aligned}$$

where the first term is controlled by choosing N sufficiently large so that $\mathcal{D}_{\{\phi_j\}_{j=1}^N} \circ \mathcal{P}_{\{\phi_j\}_{j=1}^N}$ approximates the identity on the relevant compact set and the second term is

made small by learning \mathcal{G} to approximate $\mathcal{P}_{\{\phi_j\}_{j=1}^N} \circ \mathcal{L}(g)$ from the input $\mathcal{P}_{\{\phi_j\}_{j=1}^N}(g)$. Everything else remains unchanged from [14, Theorem 2.2], and thus we conclude \square

$$\sup_{g \in \mathcal{K}} \|\mathcal{L}(g) - A(g)\|_{L^2(X)} \leq \epsilon.$$

3. Numerical Examples. In this section, we illustrate the results obtained with our architecture through two representative examples. We consider the Perron–Frobenius operator in both examples, but we can easily extend them to the Koopman operator. The first example considers the circle rotation, highlighting the recovery of spectral properties of the associated linear operator. The second example examines a nonlinearly perturbed version of Arnold’s cat map, demonstrating how the learned basis functions can adapt to the underlying system dynamics.

3.1. Data Generation. Both examples in this paper — the circle rotation and the perturbed cat map — are dynamical systems on the torus \mathbb{T}^d . We therefore require periodic observables, and we use random trigonometric polynomials to provide a rich class of training functions. To train the proposed architecture, we generate a dataset of D random trigonometric polynomial functions defined on a d -dimensional domain. Each such function is constructed as a finite linear combination of sinusoidal basis functions (sine and cosine terms) in each dimension, with randomly chosen coefficients and frequencies. Formally, a general d -dimensional trigonometric polynomial of maximum order K can be written as a linear combination of terms of the form $\prod_{j=1}^d \Psi_j(k_j x_j)$, where each $\Psi_j(\cdot)$ is either $\sin(\cdot)$ or $\cos(\cdot)$, and each integer frequency k_j ranges from 1 to K for $\sin(\cdot)$ and from 0 to K for $\cos(\cdot)$. In other words, no oscillatory component in any dimension exceeds frequency K . The coefficients in the linear combination are real numbers drawn at random uniformly in $[-1, 1]$. Note that the inclusion of $k_j = 0$ allows constant (zero-frequency) components in each dimension as well. For example, in $d = 2$ dimensions (with coordinates x_1 and x_2), such trigonometric polynomials take the form:

$$\begin{aligned} f(x_1, x_2) = & c_1 \sin(k_1 x_1) + c_2 \cos(k_2 x_2) + c_3 \sin(k_1 x_1) \sin(k_2 x_2) + c_4 \sin(k_1 x_1) \cos(k_2 x_2) \\ & + c_5 \cos(k_1 x_1) \sin(k_2 x_2) + c_6 \cos(k_1 x_1) \cos(k_2 x_2), \end{aligned}$$

with $k_1, k_2 \in \{1, \dots, K\}$ for the sine terms and $k_1, k_2 \in \{0, 1, \dots, K\}$ for the cosine terms. In higher dimensions d , a general term in the d -dimensional polynomial is a product of trigonometric functions each of the d coordinates, with frequencies up to K in each coordinate. Such functions contains a rich variety of mixed-frequency components across all dimensions.

Once the D random functions f_j are generated as described above, we apply \mathcal{L} to each of them to obtain the corresponding output functions $\mathcal{L}f_j$. This yields a training set of D input-output pairs $\{f_j; \mathcal{L}f_j\}_{j=1}^D$. In our training, $[f_j(x_1), f_j(x_2), \dots, f_j(x_n)]^\top$ serves as an input function sampled on the discretization $\{x_i\}_{i=1, \dots, n}$, and $[\mathcal{L}f_j(x_1), \mathcal{L}f_j(x_2), \dots, \mathcal{L}f_j(x_n)]^\top$ is treated as the target output. By using trigonometric polynomials as input functions, we ensure that the action of \mathcal{L} is well defined and smooth on these inputs. This property simplifies the generation of training data when $\mathcal{L}f_j$ can be computed analytically, and preserves the continuity that is important for machine-learned approximations.

In summary, our choice of trigonometric polynomials is natural because (i) they form a very expressive class of functions, which are dense in the space of continuous and square-integrable periodic functions, (ii) they are smooth, facilitating stable

training of the network (gradients can be computed reliably, and there are no discontinuities or singularities in the input data), and (iii) their generation is straightforward and computationally inexpensive.

3.2. Examples setup. We train on collections of functions as described in subsection 3.1. The size of each dataset is summarized in Table 1, where we note the number of training functions, the maximum trigonometric polynomial order, how many functions go into the validation and test sets, and the resolution of the grid.

Table 1: Data parameters for the circle rotation and perturbed cat map. We list the number of training functions (D), maximum trigonometric polynomial order (K), number of validation functions, number of test functions, and the grid size (n).

Example	D	K	Validation	Test	n
Circle rotation	1000	9	500	100	100
Perturbed cat map	3000	5	500	500	10000

Both the validation and test subsets are drawn from the same underlying class of functions as the training data generated in subsection 3.1. The training set is used to fit the model parameters by minimising the defined loss. During training, we periodically evaluate the current model on the validation set. If the validation error starts to rise while the training error keeps falling, we halt training (early stopping) to prevent overfitting. We also explore alternative hyperparameter settings—e.g. learning rate, network depth, and regularisation strength—and retain the configuration that achieves the lowest validation error. Only after all training and hyperparameter selection are complete do we assess the model on the test set. This provides an unbiased estimate of the model’s performance on unseen functions, since the test data is not used to guide model selection.

For more complex dynamics, like the nonlinearly perturbed cat map, we employ larger architectures to capture the increased complexity. The specifics of each architecture, including the dimensions, activation functions, and the number of basis learned basis functions are shown in Table 2.

Table 2: Architecture specifics for the circle rotation and perturbed cat map. We list the encoder (\mathcal{E}) and approximation networks (\mathcal{G}), their hidden layer architectures (e.g. 5×512), and activation functions. The dashes indicate that there are no hidden layers for the network \mathcal{G} since it is learning a linear map in \mathbb{R}^N .

Example	Encoder (\mathcal{E})		\mathcal{G}		N
	Hidden Layers	Activ.	Hidden Layers	Activ.	
Circle rotation	5×512	ReLU	-	Identity	30
Perturbed cat map	5×2048	ReLU	-	Identity	225

3.3. Transfer Operator with Circle rotation. The circle rotation map $T : S_1 \rightarrow S_1$ is a transformation in the circle given by $T(x) = x + \alpha \pmod{2\pi}$. For our numerical examples, we chose $\alpha = 1$. To avoid discontinuities at the endpoints of the domain interval, we embed the unit-radius circle S^1 into \mathbb{R}^2 , identifying each x with $(\cos x, \sin x) \in S^1$.

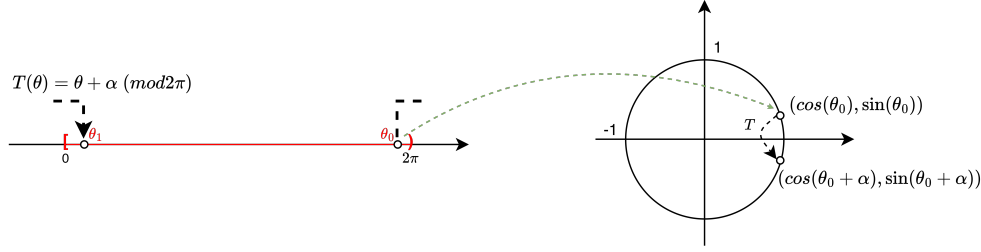


Fig. 2: Embedding of the circle-rotation map $T(\theta) = \theta + \alpha \pmod{2\pi}$ from the interval $[0, 2\pi)$ into the unit circle $S^1 \subset \mathbb{R}^2$. Each angle θ is sent to its Cartesian coordinates $(\cos \theta, \sin \theta)$, removing the discontinuity that would occur at $\theta = 0 \equiv 2\pi$ in the interval picture. The initial point θ_0 is chosen close to the right-hand endpoint of the interval to highlight the jump that is resolved by the embedding.

After parameter optimisation, we obtain both a set of basis functions spanning a subspace invariant to the transfer operator and an estimator to its action. Figure 3 displays how the learned estimator performs on unseen data for various sparsity scenarios.

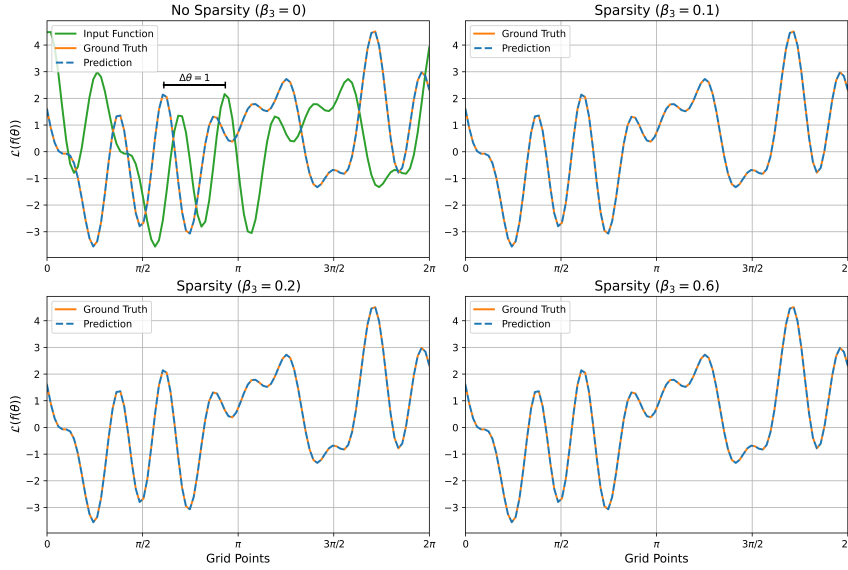


Fig. 3: Performance of the learned operator approximation on unseen input data, for different levels of sparsity.

The corresponding quantitative results—mean relative L^2 errors averaged over the test set—are summarised in Table 3.

Table 3: Mean relative L^2 error of each model on the test set.

Model	Mean relative error
No Sparsity ($\beta_3 = 0$)	6.41×10^{-4}
Sparsity ($\beta_3 = 0.1$)	6.83×10^{-4}
Sparsity ($\beta_3 = 0.2$)	6.38×10^{-4}
Sparsity ($\beta_3 = 0.6$)	7.32×10^{-4}

The approximately invariant subspace is spanned by the set of basis functions depicted in Figure 4. Each row in the heatmaps corresponds to a different basis function, while the horizontal axis represents the grid over which these functions are evaluated. By introducing a sparsity penalty, these functions gain increasingly localised support, as is evident in the more concentrated regions appearing in the heatmaps with higher penalty values.

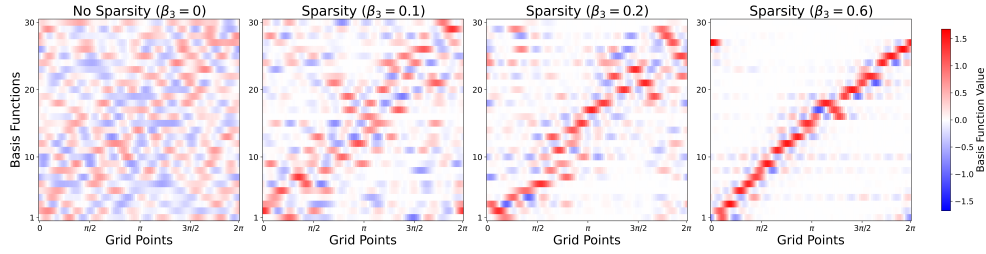


Fig. 4: Basis functions obtained under different levels of sparsity penalty. Higher sparsity encourages localisation, which is reflected in more concentrated regions of support.

After discarding functions with negligible norms and normalising the remaining ones, we examine the Gram matrix, defined as

$$G_{kj} = \langle \phi_k, \phi_j \rangle, \quad k, j = 1, \dots, N,$$

in Figure 5. The near-zero off-diagonal entries reveal that the introduction of the sparsity penalty moves the set of basis functions closer to orthogonality.

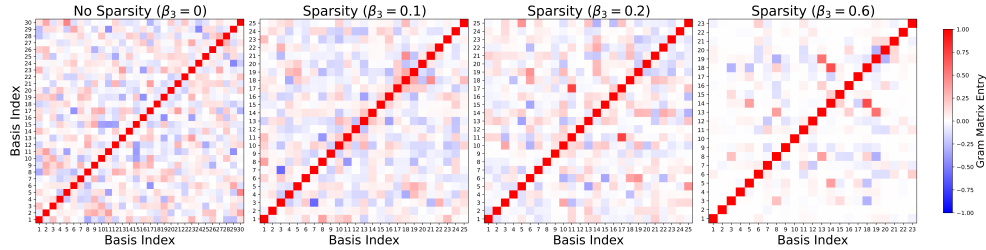


Fig. 5: Gram matrix of the filtered and normalised basis functions, highlighting that the introduction of sparsity promotes near-orthogonality (off-diagonal elements remain close to zero).

We now highlight the recovery of the operator's spectral properties through the learned estimator. By projecting onto the subspace spanned by $\{\phi_j\}_{j=1}^N$, we obtain the Galerkin system

$$L_{kj} = \langle \phi_k, \mathcal{G}(\phi_j) \rangle \quad \text{and} \quad M_{kj} = \langle \phi_k, \phi_j \rangle,$$

where M is often called the mass matrix. The approximate eigenpairs of $\hat{\mathcal{L}}$ are found by solving the generalized eigenvalue problem

$$L \mathbf{v} = \lambda M \mathbf{v}.$$

Eigenvalues and eigenvectors of (L, M) then serve as approximations to the operator's eigenpairs.

For the circle rotation, one can derive the eigenpairs analytically. The transfer operator for the circle rotation is

$$(\mathcal{L}g)(\theta) = g(\theta - \alpha).$$

Using the ansatz $\psi_k(\theta) = e^{ik\theta}$, we get

$$(\mathcal{L}\psi_k)(\theta) = e^{ik(\theta-\alpha)} = e^{-ik\alpha} \psi_k(\theta) \implies \lambda_k = e^{-ik\alpha}, \quad \psi_k(\theta) = e^{ik\theta}$$

Thus, the leading eigenvalues take the form

$$\lambda_{\pm 1} = e^{\mp i\alpha}.$$

These analytic expressions match well with our numerical experiments, which were performed with the model parameter $\beta_3 = 0.6$.

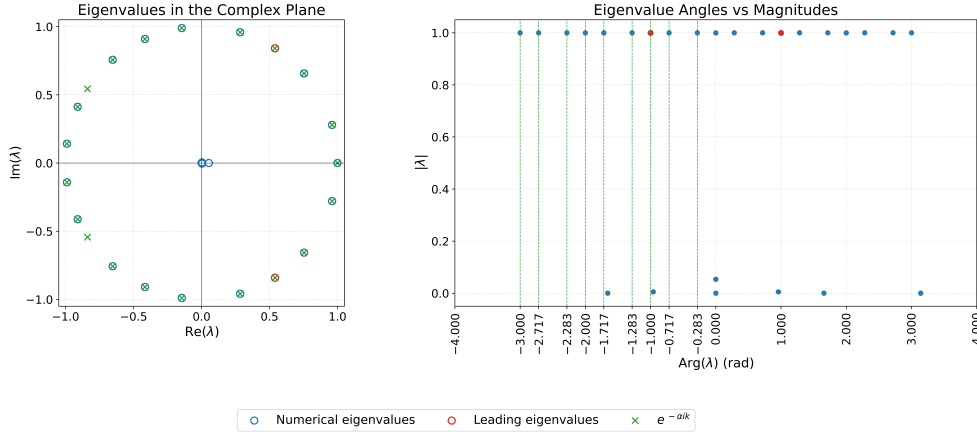


Fig. 6: **Left:** Eigenvalues of the Perron–Frobenius operator for a circle rotation by $\alpha = 1$ radians. Numerical eigenvalues (blue; leading pair corresponding to $k = \pm 1$ in red) coincide with the analytic spectrum (green). **Right:** Magnitude versus argument of the same eigenvalues. The dashed green vertical lines mark angles that are integer multiples of α , underscoring that the additional numerical eigenvalues are dynamically meaningful, but duplicate information from the lowest-order eigenvalues.

We reconstruct each leading eigenfunction from the Galerkin eigenvector $\mathbf{v} = (v_1, \dots, v_N)$ —whose entries are the coefficients in our learned basis $\{\phi_j\}_{j=1}^N$ —as

$$\psi(\theta) = \sum_{j=1}^N v_j \phi_j(\theta),$$

and find that it coincides perfectly with the analytic eigenfunction.

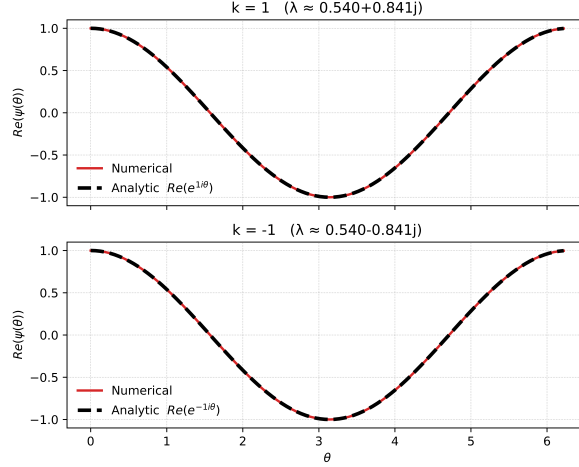


Fig. 7: Real parts of the leading eigenfunctions of the transfer operator. The analytic eigenfunction is plotted in dashed black, while its numerical counterpart in solid red. In both cases the numerical eigenfunctions coincide with the analytic curves.

Finally, we demonstrate the invariance of the learned subspace under the Perron–Frobenius operator. Recall $A := \mathcal{D}_{\{\phi_j\}_{j=1}^N} \circ \mathcal{G} \circ \mathcal{P}_{\{\phi_j\}_{j=1}^N}$ is the data-driven approximation of the Perron-Frobenius operator. On the grid $\{x_i\}_{i=1, \dots, n}$ define

$$\Phi = [\phi_j(x_i)]_{i=1, \dots, n; j=1, \dots, N} \in \mathbb{R}^{n \times N}, \quad \Psi = [A(\phi_j)(x_i)]_{i=1, \dots, n; j=1, \dots, N} \in \mathbb{R}^{n \times N},$$

and set $r = \text{rank } \Phi = \text{rank } \Psi \leq N$. We wish to determine how close the r -dimensional column space of Φ is to the r -dimensional column space of Ψ , and we do this by computing principal angles between these two subspaces. Following [12, Algorithm 6.4.3] we form the QR decomposition

$$\Phi = Q_\Phi R_\Phi, \quad \Psi = Q_\Psi R_\Psi,$$

with orthogonal $Q_\Phi, Q_\Psi \in \mathbb{R}^{n \times n}$ and upper-triangular $R_\Phi, R_\Psi \in \mathbb{R}^{n \times N}$, denote by $Q_\Phi^{(r)}$ and $Q_\Psi^{(r)}$ the first r columns of Q_Φ and Q_Ψ . If $0 \leq \theta_1 \leq \dots \leq \theta_r$ are the principal angles between the subspaces spanned by Φ and Ψ , then

$$\cos \theta_k = \sigma_k[(Q_\Phi^{(r)})^\top Q_\Psi^{(r)}], \quad k = 1, \dots, r,$$

From these angles we report three standard subspace-distance metrics:

1. the geodesic distance $d_{\max} = \max_k \theta_k$,

2. the chordal distance $d_{\text{ch}} = \|\sin \theta\|_2$,
3. the projection distance $d_{\text{pr}} = \sin d_{\text{max}}$.

 Table 4: Subspace-distance measures between $\text{span}\{\phi_j\}_{j=1}^N$ and $\text{span}\{\mathcal{A}\phi_j\}_{j=1}^N$

Metric	$\beta_3 = 0$	$\beta_3 = 0.1$	$\beta_3 = 0.2$	$\beta_3 = 0.6$
Geodesic (d_{max})	4.88×10^{-4}	4.88×10^{-4}	5.98×10^{-4}	5.98×10^{-4}
Chordal (d_{ch})	1.38×10^{-3}	1.38×10^{-3}	1.54×10^{-3}	1.29×10^{-3}
Projection (d_{pr})	4.88×10^{-4}	4.88×10^{-4}	5.98×10^{-4}	5.98×10^{-4}

Smaller values of the principal angles θ_k indicate that the two subspaces are closer, and hence the learned subspace approaches invariance under A . Across all sparsity levels β_3 , the reported distances remain on the order of 10^{-3} or less, providing strong evidence of a near-invariant learned subspace.

3.4. Transfer Operator with Perturbed Arnold’s Cat Map. We consider a nonlinear perturbation of the (linear and hyperbolic) Arnold’s cat map of the two-torus $X = \mathbb{T}^2$ introduced in [7]:

$$T : \mathbb{T}^2 \rightarrow \mathbb{T}^2, \quad T(x, y) = (2x + y + 2\delta \cos(2\pi x), x + y + \delta \sin(4\pi y + 1)) \pmod{1},$$

with $\delta = 0.01$. With this perturbation, T remains Anosov and therefore has an SRB measure μ [5, Theorem 4.12]. The spectral theory for Anosov diffeomorphisms is challenging and relies on carefully constructed anisotropic Banach spaces (e.g. [13]) that are adapted to the unstable and stable foliations. In this example, we let $\mathcal{L}f = f \circ T^{-1} / |\det DT \circ T^{-1}|$ be the Perron–Frobenius operator, and consider $\mathcal{L} : L^2(X, m) \rightarrow L^2(X, m)$ where m is Lebesgue measure on the flat torus. Note the additional determinant term in the definition of \mathcal{L} ; the constant function is no longer the leading eigenfunction of \mathcal{L} . In fact, the object μ satisfying $\mathcal{L}\mu = \mu$ is in general a *distribution* and need not lie in $L^2(\mathbb{T}^2, m)$. The probability measure (or distribution) μ describes the long-term distribution of infinitely long trajectories of T for *Lebesgue almost all* initial conditions $x \in \mathbb{T}^2$. This distribution of infinitely long trajectories is accessible through the fixed point of \mathcal{L} ; this is one of the many advantages of studying transfer operators.

To eliminate the discontinuities that arise at the edges of the unit square, we embed \mathbb{T}^2 into \mathbb{R}^4 by mapping each (x, y) to its pair of complex phases $(\cos 2\pi x, \sin 2\pi x, \cos 2\pi y, \sin 2\pi y)$. We first evaluate our model’s ability to approximate the Perron–Frobenius operator on an unseen observable. Throughout this entire example no sparsity penalty is applied ($\beta_3 = 0$). Figure 8 juxtaposes the input observable g , the ground-truth image, and our network’s prediction. The accuracy is quantified by the relative L^2 error of 1.17×10^{-2} on the full test set.

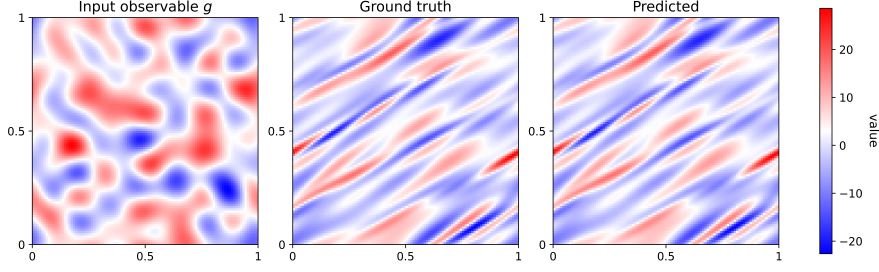


Fig. 8: Input–output approximation for the Perron–Frobenius operator of a perturbed Arnold’s cat map. The three panels show the unseen input observable g , the corresponding ground-truth response, and the network prediction. The mean L^2 relative error over the full test set is 1.17×10^{-2} .

Next, we analyse the learned set of basis functions that span the invariant subspace $V = \text{span}\{\phi_j\}_{j=1}^N$. Figure 9 shows representative basis functions obtained without sparsity penalty. Even in the absence of an explicit localisation term, the basis functions obtained through the proposed network show unmistakable alignment with contracting and expanding directions.

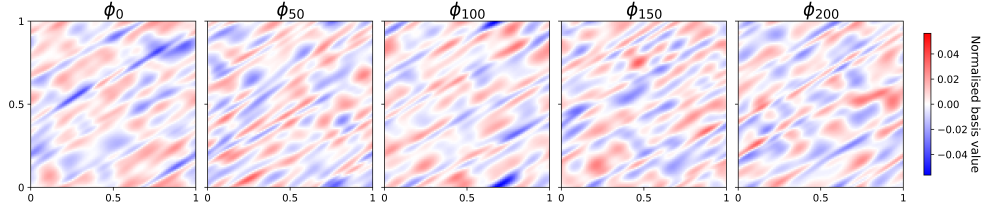


Fig. 9: Representative basis functions learned by the network. The patterns exhibit structures that align with the map’s contracting and expanding directions, illustrating how the learned invariant subspace is adapted to the underlying dynamics.

The Gram matrix of the learned basis functions is again defined by

$$G_{kj} = \langle \phi_k, \phi_j \rangle, \quad k, j = 1, \dots, N,$$

and is illustrated in Figure 10. Its nearly diagonal form shows that our training scheme implicitly promotes approximate orthogonality, even in the absence of an explicit sparsity term.

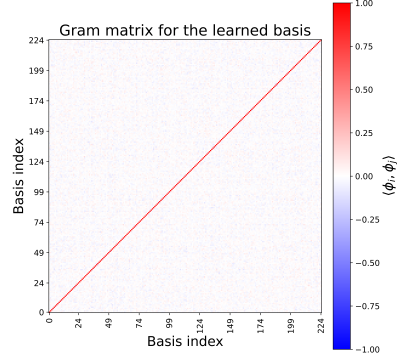


Fig. 10: Gram matrix of the learned basis functions (after ℓ^2 normalisation). The (approximately) diagonal structure shows that the network has produced a nearly orthogonal collection, despite the absence of an explicit sparsity constraint.

We now examine the spectral properties of the learned Perron–Frobenius approximator. Figure 11 displays the eigenvalues; the leading eigenvalue at $\lambda = 1$ confirms the presence of an invariant measure consistent with the SRB measure associated with this map.

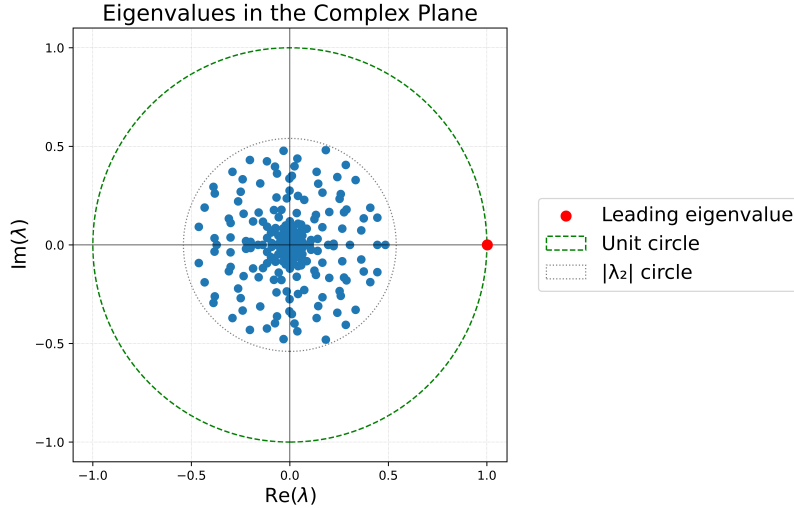


Fig. 11: Eigenvalues of the learned Perron–Frobenius operator for the model with no sparsity penalty. The leading eigenvalue (corresponding to the SRB measure) is close to 1 as expected. The remaining eigenvalues are separated away from the unit circle.

The remaining eigenvalues in Figure 11 are restricted to a disk away from the unit circle, in line with expectations if one used a correct anisotropic setup [13]. While we work in $L^2(X, m)$, we train our estimate of \mathcal{L} on smooth functions, and it is likely that this restriction to smooth functions produces the spectral gap we see in Figure 11.

Using the same Galerkin projection technique as in the previous example, we reconstruct the leading eigenfunction that represents the SRB measure and, for com-

parison, include the same leading eigenfunction reconstructed from a Fourier basis of the same dimension — built from products of sines and cosines described in subsection 3.1; see Figure 12.

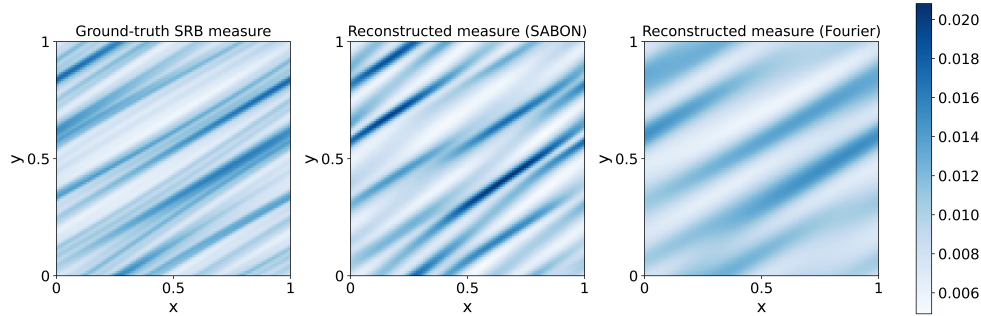


Fig. 12: Ground-truth SRB measure (left), its reconstruction using the SABON learned basis (middle), and its reconstruction using a Fourier basis of the same dimension (right).

The ground truth measure is constructed from $N = 10\,000$ Fourier basis functions, with Fejér-kernel smoothing [7]. In comparison, our reconstructed SRB measure uses 225 learned basis functions, and we compare this with the SRB measure arising from the lowest-order 225 Fourier modes. Our reconstructed SRB measure using our learned basis clearly captures more detail than a similar number of Fourier modes.

To benchmark the learned basis against the traditional Fourier basis used to construct the trigonometric polynomials in subsection 3.1, we measure the relative L^2 -projection error of the ground-truth SRB measure,

$$\varepsilon_{\mathcal{B}}^{\text{rel}} := \frac{\|\rho_{\text{SRB}} - P_{\mathcal{B}}\rho_{\text{SRB}}\|_2}{\|\rho_{\text{SRB}}\|_2}, \quad P_{\mathcal{B}} : L^2(X) \rightarrow \text{span}(\mathcal{B}) \text{ is the orthogonal projection.}$$

We compute this error for (i) the learned basis and (ii) a Fourier basis of comparable dimension. The learned basis achieves the smaller error (see Table 5).

Table 5: Relative orthogonal projection error $\varepsilon_{\mathcal{B}}^{\text{rel}} = \frac{\|\rho_{\text{SRB}} - P_{\mathcal{B}}\rho_{\text{SRB}}\|_2}{\|\rho_{\text{SRB}}\|_2}$. Lower values indicate a more accurate representation of the invariant measure.

Basis	Relative projection error
SABON (225 functions)	7.248×10^{-2}
Fourier (225 functions)	1.318×10^{-1}

Finally, we quantify and compare the invariance of the subspaces generated by the learned basis and a classical Fourier basis of the same size under the action of the Perron–Frobenius operator. We compute principal angles between each subspace and its image under the operator, summarising these in Table 6. The significantly smaller distances obtained for our learned subspace indicate superior invariance compared with the traditional Fourier basis.

Table 6: Subspace-distance measures quantifying how well the subspace is preserved under the Perron–Frobenius operator, comparing the SABON basis (225 elements, no sparsity penalty) with a Fourier basis with 225 functions. Lower values indicate greater invariance.

Metric	SABON basis	Fourier basis
Geodesic (d_{\max})	0.088	16.642
Chordal (d_{ch})	0.088	10.615
Projection (d_{pr})	0.087	1.000

A more detailed comparison is shown graphically in Figure 13, where we plot the projection distance for every individual principal angle for both subspaces.

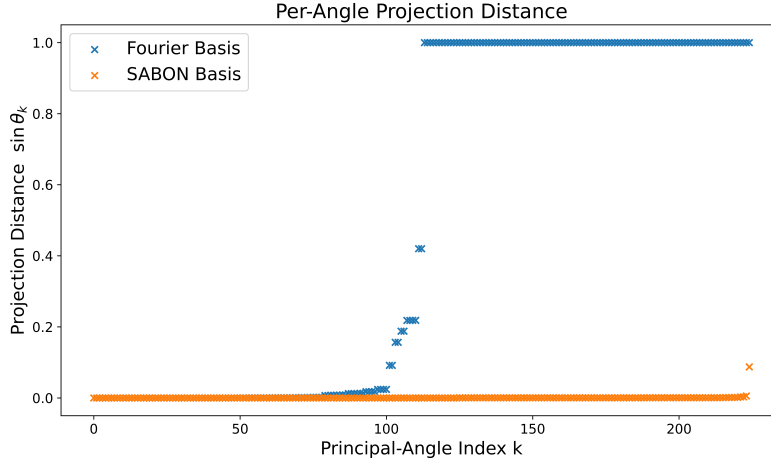


Fig. 13: Projection distance for the principal angles between each subspace and its image under the Perron–Frobenius operator for the learned basis and the Fourier basis of equal dimension. Smaller distances correspond to greater invariance.

Why does the SABON basis have far superior invariance when compared to a Fourier basis? A Fourier element—whether the complex exponential $e^{2\pi i k \cdot x}$ or the purely real sine–cosine products introduced in subsection 3.1—is aligned with coordinate axes. The contracting dynamics of T means that the frequency of a Fourier mode will be increased in stable directions of the dynamics under application of \mathcal{L} . Thus those modes in the Fourier basis with higher frequencies may be pushed far out of the original span of the Fourier modes, and made near-orthogonal to the Fourier basis. Indeed, Figure 13 indicates that this occurs to more than half of the Fourier modes.

The SABON basis, on the other hand, is learned jointly with the dynamics, so the network discovers functions that organise along the stable and unstable directions. The resulting modes resemble elongated ridges: long in the expanding direction and sharply confined in the contracting one. When such a ridge is pushed forward by \mathcal{L} it tends to become another ridge, aiding the invariance of the SABON subspace. This anisotropic feature, absent from the isotropic Fourier family, accounts for the much

smaller distances reported for SABON in Table 6 and illustrated in Figure 13.

A further crucial aspect of our learned SABON basis is its *efficiency*. As mentioned above, our learned basis functions tend to align with the stable and unstable directions arising from the dynamics. This yields basis functions that have more rapid oscillation in stable directions and slower oscillation in unstable directions, which is exactly the form one expects for eigendistributions [13]. With a comparable number of basis functions, our learned functions can therefore more accurately represent the eigenprojectors.

4. Conclusions. We have introduced the Single Autoencoder Basis Operator Network (SABON)—a neural framework that jointly learns

- an operator approximation $\hat{\mathcal{L}}$ of a Koopman or Perron–Frobenius operator \mathcal{L} and
- a data-driven basis $\{\phi_j\}_{j=1}^N$ whose span $V = \text{span}\{\phi_j\}_{j=1}^N$ is approximately invariant under \mathcal{L} .

SABON cleanly achieves this by combining an encoder–decoder structure with a linear latent map \mathcal{G} and a composite loss that balances reconstruction accuracy, operator approximation accuracy, and sparsity. We proved a universal approximation theorem in the spirit of Hua [14], but specialised to a single neural basis that targets transfer and Koopman operators.

Two canonical examples were used to highlight key features of SABON:

1. **Circle rotation.** The SABON basis provided accurate reconstruction of the analytic eigenpairs and recovered the rotation angle α directly from the leading eigenvalues, while the associated eigenfunctions coincide with the theoretical $e^{ik\theta}$ modes. This example provided evidence that the learned basis accurately captured the main dynamical features of the system.
2. **Perturbed Arnold cat map.** For a nonlinear uniformly hyperbolic map SABON’s learned basis outperformed a traditional Fourier basis, by adapting to the geometry inherent in the dynamics. This is particularly surprising given the well-known theoretical approximation strengths of Fourier modes. The network discovered basis functions largely aligned with the contracting and expanding directions, leading to more accurate estimates of the physical invariant measure of the dynamics and a highly invariant approximation subspace.

Future directions. Promising paths for further research include:

- learning the operator spectrum directly in latent space, bypassing external Galerkin projections;
- investigating additional examples where isotropic bases fail and data-adaptive bases excel;
- extending SABON to high-dimensional or partially observed systems to assess scalability and sample efficiency;
- deriving quantitative rates that relate network width, depth and sparsity to the operator approximation error.

Acknowledgments. The research of GF is supported by an Australian Research Council (ARC) Laureate Fellowship FL230100088. The research of KK is supported by a UNSW University International Postgraduate Award, with additional funding from UNSW’s School of Mathematics and Statistics and the ARC Laureate Fellowship. Computational resources were generously provided by Katana infrastructure at UNSW [24], which significantly facilitated this research.

REFERENCES

- [1] A. AMINI, C. ZHENG, Q. SUN, AND N. MOTEE, *Carleman linearization of nonlinear systems and its finite-section approximations*, 2025, <https://doi.org/10.3934/dcdsb.2024102>, <https://www.aims sciences.org/article/id/66bb1050c19d0835a27a7ed7>.
- [2] H. ARBABI AND I. MEZIĆ, *Ergodic theory, dynamic mode decomposition, and computation of spectral properties of the koopman operator*, SIAM Journal on Applied Dynamical Systems, 16 (2017), pp. 2096–2126, <https://doi.org/10.1137/17M1125236>, <https://doi.org/10.1137/17M1125236>, <https://arxiv.org/abs/https://doi.org/10.1137/17M1125236>.
- [3] K. BHATTACHARYA, B. HOSSEINI, N. B. KOVACHKI, AND A. M. STUART, *Model Reduction And Neural Networks For Parametric PDEs*, The SMAI Journal of computational mathematics, 7 (2021), pp. 121–157, <https://doi.org/10.5802/smai-jcm.74>, <https://smai-jcm.centre-mersenne.org/articles/10.5802/smai-jcm.74/>.
- [4] N. BOULLÉ AND A. TOWNSEND, *A mathematical guide to operator learning*, Elsevier, 2024, p. 83–125, <https://doi.org/10.1016/bs.hna.2024.05.003>, <http://dx.doi.org/10.1016/bs.hna.2024.05.003>.
- [5] R. BOWEN, *Equilibrium states and the ergodic theory of anosov diffeomorphisms*, Lecture notes in mathematics, 470 (1975).
- [6] T. CHEN AND H. CHEN, *Universal approximation to nonlinear operators by neural networks with arbitrary activation functions and its application to dynamical systems*, IEEE Transactions on Neural Networks, 6 (1995), pp. 911–917, <https://doi.org/10.1109/72.392253>.
- [7] H. CRIMMINS AND G. FROYLAND, *Fourier approximation of the statistical properties of Anosov maps on tori*, Nonlinearity, 33 (2020), pp. 6244–6296.
- [8] T. EISNER, B. FARKAS, M. HAASE, AND R. NAGEL, *Operator Theoretic Aspects of Ergodic Theory*, Springer International Publishing, 2015, <https://doi.org/10.1007/978-3-319-16898-2>, <http://dx.doi.org/10.1007/978-3-319-16898-2>.
- [9] G. FROYLAND, D. GIANNAKIS, B. R. LINTNER, M. PIKE, AND J. SLAWINSKA, *Spectral analysis of climate dynamics with operator-theoretic approaches*, Nature Communications, 12 (2021), <https://doi.org/10.1038/s41467-021-26357-x>, <http://dx.doi.org/10.1038/s41467-021-26357-x>.
- [10] D. GIANNAKIS, J. SLAWINSKA, AND Z. ZHAO, *Spatiotemporal feature extraction with data-driven koopman operators*, in Proceedings of the 1st International Workshop on Feature Extraction: Modern Questions and Challenges at NIPS 2015, D. Storcheus, A. Rostamizadeh, and S. Kumar, eds., vol. 44 of Proceedings of Machine Learning Research, Montreal, Canada, 11 Dec 2015, PMLR, pp. 103–115, <https://proceedings.mlr.press/v44/giannakis15.html>.
- [11] C. GIN, B. LUSCH, S. L. BRUNTON, AND J. N. KUTZ, *Deep learning models for global coordinate transformations that linearise pdes*, European Journal of Applied Mathematics, 32 (2021), p. 515–539, <https://doi.org/10.1017/S0956792520000327>.
- [12] G. H. GOLUB AND C. F. VAN LOAN, *Matrix computations*, JHU press, 2013.
- [13] S. GOUÉZEL AND C. LIVERANI, *Banach spaces adapted to anosov systems*, Ergodic Theory and dynamical systems, 26 (2006), pp. 189–217.
- [14] N. HUA AND W. LU, *Basis operator network: A neural network-based model for learning nonlinear operators via neural basis*, Neural Networks, 164 (2023), pp. 21–37, <https://doi.org/https://doi.org/10.1016/j.neunet.2023.04.017>, <https://www.sciencedirect.com/science/article/pii/S0893608023002034>.
- [15] S. KLUS, F. NÜSKE, P. KOLTAI, H. WU, I. KEVREKIDIS, C. SCHÜTTE, AND F. NOÉ, *Data-driven model reduction and transfer operator approximation*, Journal of Nonlinear Science, 28 (2018), pp. 985–1010, <https://doi.org/10.1007/s00332-017-9437-7>, <https://doi.org/10.1007/s00332-017-9437-7>.
- [16] B. O. KOOPMAN, *Hamiltonian systems and transformation in hilbert space*, Proceedings of the National Academy of Sciences, 17 (1931), pp. 315–318, <https://doi.org/10.1073/pnas.17.5.315>, <https://www.pnas.org/doi/abs/10.1073/pnas.17.5.315>, <https://arxiv.org/abs/https://www.pnas.org/doi/pdf/10.1073/pnas.17.5.315>.
- [17] N. KOVACHKI, Z. LI, B. LIU, K. AZIZZADENESHELI, K. BHATTACHARYA, A. STUART, AND A. ANANDKUMAR, *Neural operator: learning maps between function spaces with applications to pdes*, J. Mach. Learn. Res., 24 (2023).
- [18] H.-G. LEE, *Linearization of Nonlinear Control Systems*, Springer Nature Singapore, 2022, <https://doi.org/10.1007/978-981-19-3643-2>, <http://dx.doi.org/10.1007/978-981-19-3643-2>.
- [19] Z. LI, N. KOVACHKI, K. AZIZZADENESHELI, B. LIU, K. BHATTACHARYA, A. STUART, AND A. ANANDKUMAR, *Fourier neural operator for parametric partial differential equations*, 2020, <https://doi.org/10.48550/ARXIV.2010.08895>, <https://arxiv.org/abs/2010.08895>.

- [20] L. LU, P. JIN, G. PANG, Z. ZHANG, AND G. E. KARNIADAKIS, *Learning nonlinear operators via deeponet based on the universal approximation theorem of operators*, Nature Machine Intelligence, 3 (2021), p. 218–229, <https://doi.org/10.1038/s42256-021-00302-5>, <http://dx.doi.org/10.1038/s42256-021-00302-5>.
- [21] B. LUSCH, J. N. KUTZ, AND S. L. BRUNTON, *Deep learning for universal linear embeddings of nonlinear dynamics*, Nature Communications, 9 (2018), p. 4950, <https://doi.org/10.1038/s41467-018-07210-0>, <https://doi.org/10.1038/s41467-018-07210-0>.
- [22] I. MEZIĆ, *Analysis of fluid flows via spectral properties of the koopman operator*, Annual Review of Fluid Mechanics, 45 (2013), p. 357–378, <https://doi.org/10.1146/annurev-fluid-011212-140652>, <http://dx.doi.org/10.1146/annurev-fluid-011212-140652>.
- [23] R. L. PEGO, *Compactness in l_2 and the fourier transform*, Proceedings of the American Mathematical Society, 95 (1985), pp. 252–254, <http://www.jstor.org/stable/2044522> (accessed 2025-05-02).
- [24] PVC (RESEARCH INFRASTRUCTURE), UNSW SYDNEY, *Katana*, 2010, <https://doi.org/10.26190/669X-A286>, <https://researchdata.edu.au/katana/1733007>.
- [25] P. J. SCHMID, *Dynamic mode decomposition of numerical and experimental data*, Journal of Fluid Mechanics, 656 (2010), p. 5–28, <https://doi.org/10.1017/S0022112010001217>.
- [26] N. TAKEISHI, Y. KAWAHARA, AND T. YAIRI, *Learning koopman invariant subspaces for dynamic mode decomposition*, in Advances in Neural Information Processing Systems, I. Guyon, U. V. Luxburg, S. Bengio, H. Wallach, R. Fergus, S. Vishwanathan, and R. Garnett, eds., vol. 30, Curran Associates, Inc., 2017, https://proceedings.neurips.cc/paper_files/paper/2017/file/3a835d3215755c435ef4fe9965a3f2a0-Paper.pdf.
- [27] M. O. WILLIAMS, I. G. KEVREKIDIS, AND C. W. ROWLEY, *A data-driven approximation of the koopman operator: Extending dynamic mode decomposition*, Journal of Nonlinear Science, 25 (2015), p. 1307–1346, <https://doi.org/10.1007/s00332-015-9258-5>, <http://dx.doi.org/10.1007/s00332-015-9258-5>.